Technical Note

An On-Orbit Relative Sensor Normalization for Unbalance Images from the Ice Pathfinder Satellite (BNU-1)

Sishi Zhang [1], **Xinyi Shang** [1], **Lanjing Li** [2,3,4], **Ying Zhang** [1], **Xiaoxu Wu** [1], **Fengming Hui** [2,3,4], **Huabing Huang** [2,3,4] **and Xiao Cheng** [2,3,4,*]

1   State Key Laboratory of Remote Sensing Science, College of Global Change and Earth System Science, Beijing Normal University, Beijing 100875, China; 201931490002@mail.bnu.edu.cn (S.Z.); 201931490008@mail.bnu.edu.cn (X.S.); 201831490009@mail.bnu.edu.cn (Y.Z.); wuxx@bnu.edu.cn (X.W.)
2   School of Geospatial Engineering and Science, Sun Yat-sen University, Zhuhai 519000, China; lilj58@mail2.sysu.edu.cn (L.L.); huifm@mail.sysu.edu.cn (F.H.); huanghb55@mail.sysu.edu.cn (H.H.)
3   Key Laboratory of Comprehensive Observation of Polar Environment (Sun Yat-sen University), Ministry of Education, Zhuhai 519082, China
4   Southern Marine Science and Engineering Guangdong Laboratory (Zhuhai), Zhuhai 519082, China
*   Correspondence: chengxiao9@mail.sysu.edu.cn

Abstract: The Ice Pathfinder satellite (code: BNU-1) is the first Chinese microsatellite, designed for monitoring polar climate and environmental changes. The major payload of BNU-1 is the wide-field camera which provides multispectral satellite images with a 73.69 m spatial resolution and a 739 km swath width. However, the color misrepresentation issue can be observed as the BUN-1 image appears yellowish as it gets farther towards the center field of view (FOV). The blue band of the image appears to be higher near the center FOV and declines generously towards both the edge areas of the image, which may cause the color misrepresentation issue. In this study, we develop a relative sensor normalization method to reduce the radiance errors of the blue band of BNU-1 images. This method uses the radiometric probability density distribution of the BNU-1 panchromatic band as a reference, correcting the probability density distribution of the blue band radiance first. Then, the mean adjustment is used to correct the mean of the blue band radiance after probability density function (PDF) correction, obtaining the corrected radiance in the blue band. Comparisons with the ground measurements and the Landsat8 image reveal the following: (1) The radiances of snow surfaces also have good consistency with ground observations and Landsat-8 images in the red, green, and blue bands. (2) The radiance errors of the uncorrected BNU-1 images are eliminated. The RMSE decreases from 80.30 to 32.54 $W/m^2/\mu m/sr$. All these results indicate that the on-orbit relative correction method proposed in this study can effectively reduce the radiance errors of the BNU-1 images.

Keywords: Ice Pathfinder satellite (BUN-1); relative radiometric correction; histogram matching; unbalance images

1. Introduction

Under the combined influence of global warming and human activities, the polar environment is undergoing rapid and drastic changes [1–3]. The development of satellite remote sensing technology has provided the possibility for wide-scale, rapid, and real-time monitoring of global environmental changes [4–6]. Optical remote sensing has abilities of acquiring large-scale, high-resolution visual images, making it the most representative and widely used remote sensing technique for polar observations [7]. Optical remote sensing images have been widely used for recording land cover changes, monitoring ice sheet and sea ice motions, and other applications in the polar regions [8,9].

Due to the fact that the revisit of sun-synchronous orbit satellite observation often exceeds 1 day/time, and the effective observation of visible remote sensing is greatly affected

by weather conditions such as clouds and rain, the development trend of satellite technology is to conduct networked observations by launching multiple low-cost microsatellites. Microsatellites are a type of satellite with a mass less than 500 kg. They have comparable functions to similar large-scale satellites, and have advantages such as flexible launch methods, high function density, simple structure, light weight, and small size. Based on these advantages, it is easy to construct a satellite constellation with microsatellites which have a shorter revisit period within 24 h. In the first half of 2021 alone, a total of 1262 satellites were launched globally, of which over 1100 were microsatellites, accounting for nearly 90%. SpaceX's second-generation Starlink plan anticipates launching 29,988 microsatellites. Amazon's "Project Kuiper" aims to launch 3296 microsatellites. The global microsatellite industry is experiencing explosive growth.

"Ice Pathfinder" (code: BNU-1) is the first satellite of the microsatellite constellation designed for monitoring polar climate and environmental changes. It was successfully launched at the Taiyuan Satellite Launch Center in Shanxi province, China, on 12 September 2019. It carries three payloads: a wide-field camera, a narrow-field high-resolution camera, and a ship AIS receiver [10]. (Table 1). The major payload of BNU-1 is the wide-field camera which provides multispectral satellite images with a 73.69 m spatial resolution and a 739 km swath width.

Table 1. Main parameters of the payloads of BNU-1.

Payloads		Main Parameters
The wide-field camera	Parameters	Panchromatic, multispectral, push broom
	Spatial Resolution	73.69 m
	Swath Width	739 km
	Spectral bandwidth	Panchromatic: 527 nm~769 nm Blue (B1): 471 nm~506 nm Green (B2): 560 nm~599 nm Red (B3): 638 nm~676 nm
The narrow-field high-resolution camera	Image mode	Area array staring.
	Spatial Resolution	8.2 m
	Swath Width	739 km
	Spectral bandwidth	Bayer RGB
The ship AIS receiver	Receiving frequency point	161.975 MHz, 162.025 MHz 156.775 MHz, 156.825 MHz
	Modulation mode	GMSK/FM
	Receiving sensitivity	≤ -112 dBm

Visible sensors carried by BNU-1 have the advantages of high coverage and relatively high spatial resolution, which have abilities of obtaining high-quality optical remote sensing images. However, due to the distributions of dark, noise, heat, and other environmental factors, the radiometric response of complementary metal-oxide-semiconductor (CMOS) sensors is also unbalance, often leading to the appearance of nonlinear radiometric errors in the remote sensing images. The radiometric consistency of satellite images is essential to obtain the whole image mosaics for Greenland or Antarctic ice sheets or monitor sea ice changes for Arctic or Antarctic regions [8,11]. For example, the distributions of bule ice, which are widely distributed in Antarctic, maybe failed to be obtained if the radiometric errors are contained in the original satellite images [12]. Therefore, before applying visible remote sensing images, the radiometric errors need to be evaluated and corrected [13].

Existing radiometric correction methods can be divided into two categories. The first category is radiometric calibration, which can be divided into laboratory calibration, on-orbit calibration, and field calibration [14]. Laboratory calibration uses a stable light source for accurate radiometric calibration of the target payload. On-orbit calibration includes active
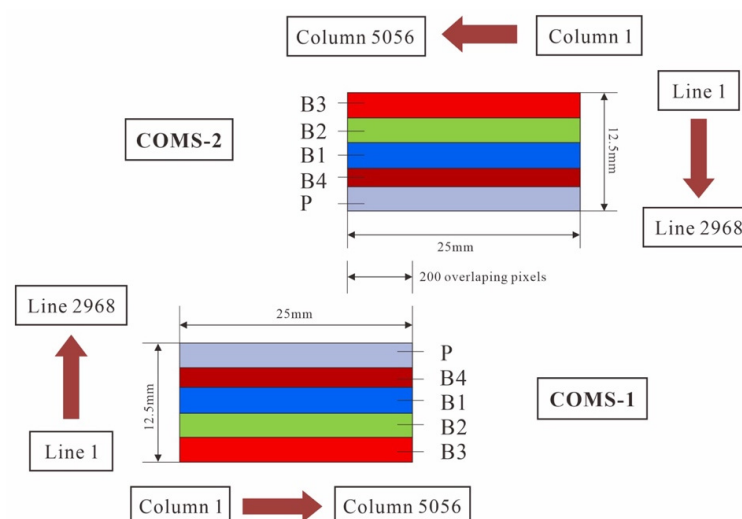
onboard calibration and passive sun calibration. Field calibration serves as an alternative method to compensate for changes in the on-orbit sensor by selecting scenes. It requires observers to conduct on-site surveys to measure the surface radiances for a selected area with a large flat terrain, high visibility, and uniform reflectance. Then, these measurements are used to calibrate the observation from the satellite. The second category of methods is the relative sensor normalization. Common relative sensor normalization methods include histogram matching, histogram equalization, and moment matching [15,16]. These methods assume that detectors from different satellite sensors should have the same radiation distribution characteristics for the detected objects. They remove errors by calculating the correlation between the error band and the grayscale statistics of the normal image.

The wide-field camera carried by BNU-1 is a visible remote sensing sensor. It is also necessary to evaluate and correct the radiometric errors of the images obtained by BNU-1. This study first explores the characters of the radiometric errors of BNU-1 images and then tries to correct these errors, using a relative sensor normalization method. The corrected images are finally evaluated by comparing them with the Landsat8 OLI images and the field observations.

2. Data and Methods

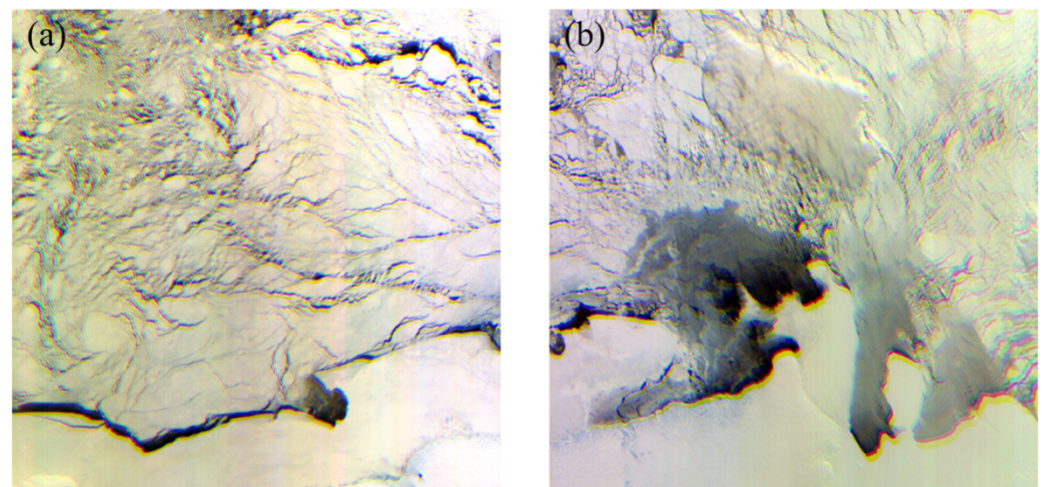### 2.1. Introduction to the Wide-Field Camera Carried by BNU-1

The wide-field camera uses sensor coating technology and complementary metal-oxide-semiconductor (CMOS) high-frame-rate digital time-delay integration (TDI) technology to achieve push-broom imaging in one panchromatic band and four multispectral bands (blue, green, red, and red edge). The camera's focal plane is composed of two CMOS sensors (pixel size of 4.25 μm, effective pixel count of 5056 (H) × 2968 (V)) stitched together to achieve wide coverage and bi-directional scanning capability, with adjacent CMOS sensors overlapping by 200 pixels, as shown in Figure 1. The camera uses the substrate of the main frame of the focal plane electronics box as the main load-bearing structure of the camera, which improves the overall stiffness of the focal plane electronics box, saves the weight and volume of the entire system, and achieves miniaturization. In addition to the standard operating mode suitable for routine tasks, the wide-field camera also has a high dynamic range (HDR) operating mode. This mode is suitable for observing the details of specific objects in high dynamic scenes. In this mode, the sensor automatically performs two long and short exposures of the same object, and the output fused image can effectively improve the imaging effect of high dynamic scenes where ice, snow, and land water coexist.

Figure 1. BNU-1 wide-field camera focal plane layout diagram. The wide-field camera focal plane is composed of two CMOS sensors. Every CMOS can capture an image of 5056 × 2968 pixels per shot. Two CMOSs can capture two images per shot. These two images have 200 overlapping pixels that represent the same object on the ground.
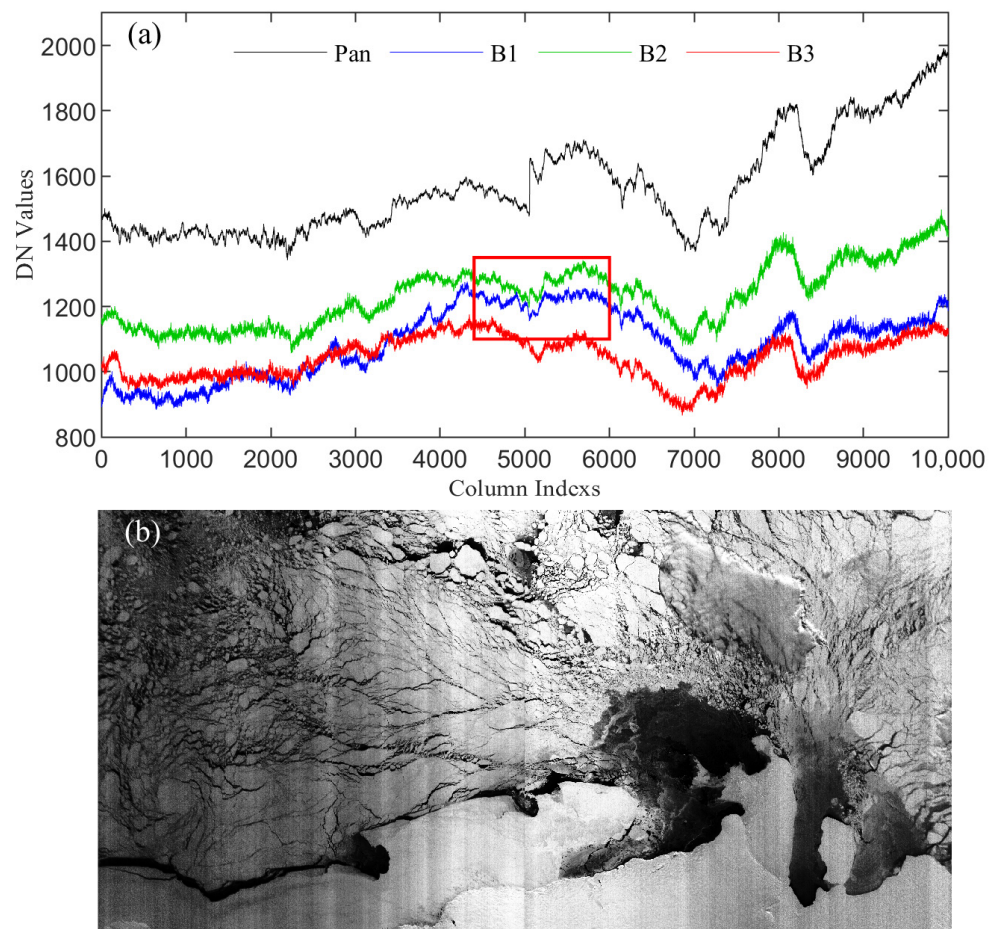
2.2. BNU-1 Data

Since its launch, BNU-1 has acquired over 20,000 images of polar regions. These images were received from the ground stations from the satellite directly. We call these images BNU-1 level-0 images. BNU-1 level-0 images contains the observations in panchromatic (P), blue (B1), green (B2), red (B3), and red-edge spectral (B4) bands which are recorded as digital number (DN) values. The DN images of B1, B2, and B3 bands can be used to compose true RGB color images. Figure 2 shows two RGB color composite images of Amery Ice Shelf, Antarctica Synchronously acquired by the CMOS1 and CMOS2 sensors of BNU-1 on 8 October 2019 (Orbit Number: 200214500). The color misrepresentation issue can be observed as the image appears purplish as it gets closer to the center field of view (FOV) and appears yellowish as it gets farther to the center FOV (Figure 2). A similar issue also appeared in the other BNU-1 level-0 images.

Figure 2. Two RGB color composite images in Amery Ice Shelf, Antarctica acquired by BNU-1. (**a**,**b**) are acquired by the CMOS1 and CMOS2 sensors, respectively. The bright pixels in the images represent ice and snow surfaces, while the dark pixels represent water bodies.

To address the color misrepresentation issue, several series of the DN values extracted cross the satellite flight direction from P, B1, B2, and B3 bands are shown in Figure 3a. The corresponding BNU-1 image in B1 band is shown in Figure 3b. The image shown in Figure 3b was stitched together using images from the CMOS1 and CMOS2 sensors. The numbers of 1-5056 columns of the image are from the CMOS1 sensor, while the numbers of 5057-10112 columns are from the CMOS2 sensor. As shown in Figure 3a, great consistency is observed between the two multispectral bands (B2 and B3) and the panchromatic band (the black line in Figure 3a). However, the values of the blue (B1) band exhibit abnormal changes in the center FOV and in the off-center FOVs. The B1 band appears to be higher near the center FOV and declines generously towards both the edge areas of the mosaic image, which may cause the color misrepresentation issue shown in Figure 2. It is worth noting that the DN values in the blue band perform even lower than that in the red band in the first 3000 s columns (Figure 3a), which indicates a further correction procedure is required. The red box highlights where the values in the B1 band perform troublesome due to the higher DN values near the center FOV, while the rest of the DN values due to lower column values. Similar DN offsets are observed in the BNU-1 imagery acquired in the North Pole region, but the trend of the column means that the blue band is flipped, since to the scanning mode is switched between both polar regions.
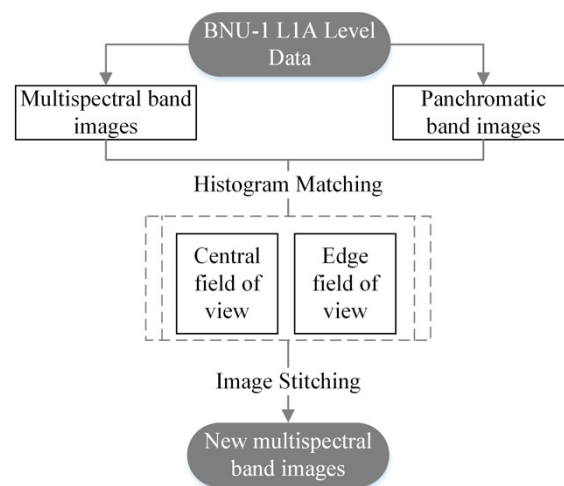
Figure 3. (**a**) The curves of DN values of the rows of the panchromatic band (B0) and three multispectral bands (B1–B3) for the mosaic image for the Antarctic region shown in Figure 2. The red box highlights the DN values are the row mean DN values from the center columns of the CMOS1 and CMOS2 images; (**b**) Single band mosaic image of the mosaic image for the Antarctic region shown in Figure 2. The mosaic image is composed of band B1 of two CMOS images (**Left**: CMOS1 and **Right**: CMOS2).

After a vast amount of image data reviewing, it was found that the intensity performs good uniformity in the panchromatic bands of both the CMOS1 and CMOS2 sensors that are carried on the BNU-1 satellite, while the obvious unbalance intensity existed over the true color composite images. The intensity of B1 band appeared to be higher surrounding the centerline and declined generously towards both the edge areas of the image. Therefore, it is necessary to have a relative sensor normalization for BNU-1 images to correct radiometric errors before their applications.
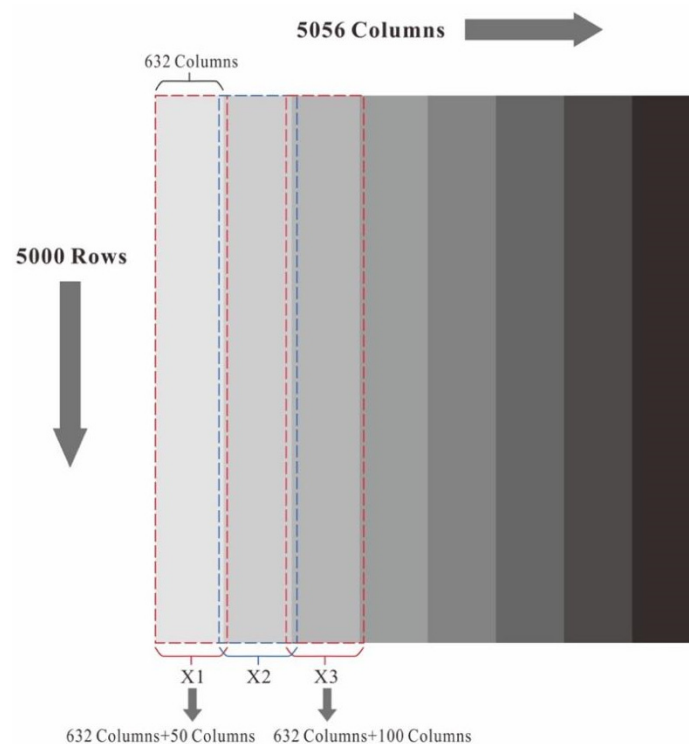
2.3. The Relative Radiometric Correction

A relative sensor normalization method was presented based on the single-scene statistics, combined with the traditional histogram matching method. The method includes four principal steps: image cropping, histogram matching, mean adjustment, and image stitching. The B1 band image along with the panchromatic image were used as an example to present the data processing workflow that is illustrated as Figure 4.

Figure 4. Flow diagram for the improved histogram matching algorithm.

(1) Image cropping

The B1 image and the panchromatic image both have identical dimensions, which are 5000 rows by 5056 columns. Both images are divided into 8 strips evenly along the column direction. As shown in Figure 5, from left to right the strip i is denoted as {Xi} for the B1 image and {Yi} for the panchromatic image. Each strip is expanded with 50 pixels towards both sides, except the strips {X1} and {X8} as well as {Y1} and {Y8}, which only expanded 50 pixels towards the inner side. Once the image cropping is completed, the parameters such as center FOV and the edge FOV of the image are specified. X1 is the center FOV when the camera is operated in a forward scanning mode, while X8 is the center FOV when the camera is in a reverse scanning mode. It is notable that the imaging cameras CMOS1 and CMOS2 move forward and backward, respectively, in the northern hemisphere. The scanning modes are switched in the southern hemisphere.

Figure 5. Schematic diagram of image cropping.

(2) Histogram matching

In this study, the B1 image is considered as the source image and the panchromatic image is the target image. A histogram is constructed both for the source strip image $\{X_i\}$, and the target strip image $\{Y_i\}$. The correction coefficients for $\{X_i\}$ are determined by matching its histogram to the corresponding target histogram constructed from $\{Y_i\}$.

Assuming the pixel gray level in a source histogram is k (k = 0, 1, 2, ..., K), the probability density (P_k) of the source strip image where gray-level value is equal to k can be calculated as follows:

$$P_k = \frac{m_k}{M} \tag{1}$$

where m_k is the number of pixels with gray level equal to k. M is the total number of pixels in the source strip image. Therefore, the cumulative probability density (S_k) for the source strip image is as follows:

$$S_k = \sum_{j=0}^{k} P_k(j) \tag{2}$$

Assuming the pixel gray level in a target histogram is l (l = 0, 1, 2, ..., L), the probability density (P_l) of the target strip image where gray-level value is equal to l can be calculated as follows:

$$P_l = \frac{m_l}{M} \tag{3}$$

where m_l is the number of pixels with gray-level value equal to l. M is the total number of pixels in the target strip image. Therefore, the cumulative probability density (V_l) for the target strip image is as follows:

$$V_l = \sum_{j=0}^{l} P_l(j) \tag{4}$$

If the cumulative probability density of the source histogram and the target histogram meet the following criteria:

$$V_l \leq S_k \leq V_{l+1} \tag{5}$$

$$|V_l - S_k| - |V_{l+1} - S_k| \leq 0 \tag{6}$$

then the gray-level k of the source histogram is replaced with the gray-level l of the target histogram. If only Equation (5) is met, then the gray-level k of the source histogram is replaced with the gray-level l + 1 of the target histogram. Hence, the strip source image $\{X_i\}$ is denoted as $\{Z_i\}$ after histogram matching.
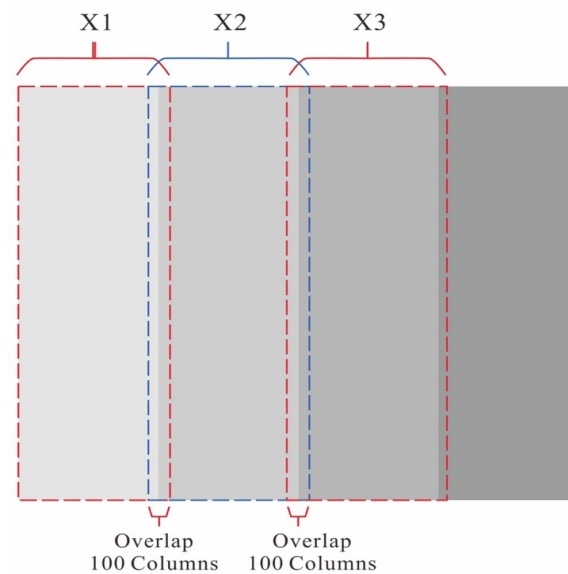
(3) Mean Adjustment

Mean adjustment is conducted based upon two assumptions as follows: (1) there are no errors existing in the DN values of the center FOV $\{X_1\}$ and (2) the mean adjustment results to the constant proportional changes from $\{Z_i\}$ to $\{Z_i'\}$, which can be represented using an adjustment coefficient. Therefore, the new strip image $\{Z_i'\}$ can be calculated as follows:

$$\frac{Z_1}{X_1} = T = \frac{Z_2}{Z_2'} = \cdots = \frac{Z_8}{Z_8'} \tag{7}$$

(4) Image stitching

After adjusting the mean value, the strip $\{Z_i'\}$ are stitched together with a 100-column overlapping (Figure 6). The average value is only calculated where the overlapping exists between adjacent strips and is used to replace with the original values in $\{Z_i'\}$, while the values remain the same for the remaining region of $\{Z_i'\}$.
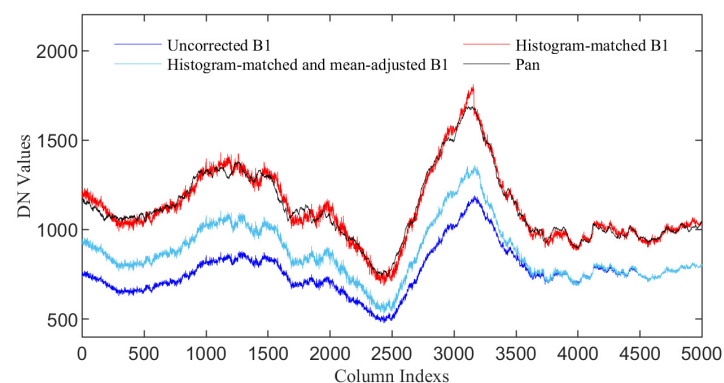
Figure 6. Schematic diagram of image stitching.

3. Results

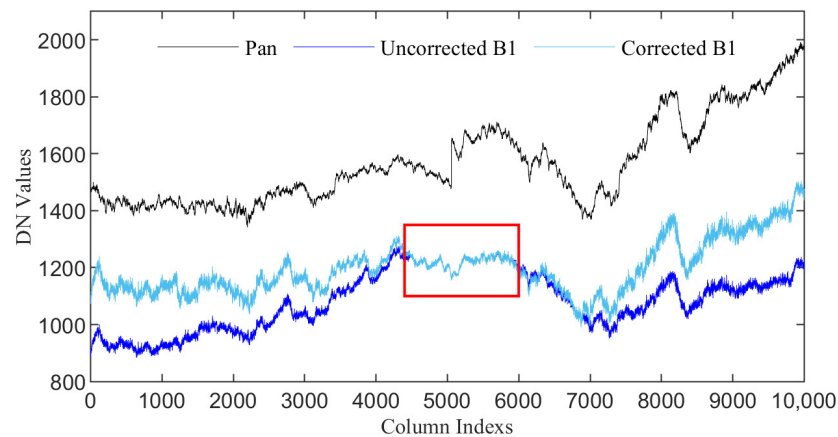### 3.1. Performances of the Relative Radiometric Correction

Figure 7 shows the changes in DN value curves of a BNU-1 image in B1 band when the relative sensor normalization has been applied to correct its radiometric errors. The BNU-1 image was acquired on 5 July 2020 (orbit number: 2000021032). The black line in Figure 7 is the DN value curve of the BNU-1 image in P band, which is considered as the curve without deviation. The bule line in Figure 7 is the DN value curve of the original BNU-1 image in B1 band. An obvious negative deviation can be found in the curve from 0 to 4000 columns. Then, histogram matching is used to correct the deviation. A red curve in Figure 7 is obtained when the histogram of the B1 band is matched to the histogram of the P band. The red curve is very consistent with the black curve. But it retains many detail fluctuations, such as a DN value peak near 3200 columns. Since the radiances in different bands are different, we must apply the mean adjustment to the red curve. In this case, the radiance difference between the B1 and P band is defined as the mean difference of DN values in B1 and P band from 4324 to 5056. The cyan curve is the final DN value curve of the corrected BNU-1 image in B1 band. The negative deviation has been improved in the cyan curve.
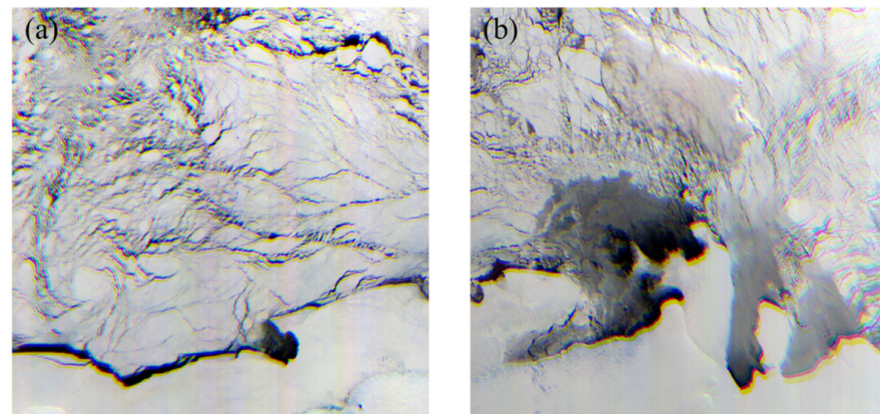

Figure 7. The DN value curves of the original and corrected image. The DN value of every column is averaged in rows. The image was acquired on 5 July 2020 (orbit number: 2000021032). The bule curve shows the DN values from the uncorrected B1 band. The red curve shows the DN values from the B1 band after histogram matching. The cyan curve shows the DN values from the B1 band after histogram matching and mean adjustment, which is the corrected image. The black curve shows the DN values from the P band.
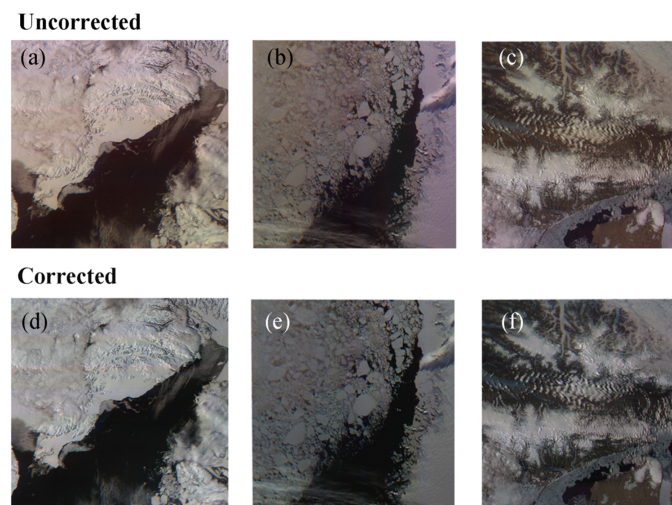
3.2. Results of the Corrected BNU-1 Images

The relative sensor normalization has been applied to improve the radiometric errors of BNU-1 level-0 images. As shown in Figure 3, obvious differences are observed between the original blue band and the panchromatic band. The DN values from the panchromatic band change relatively smoothly, and the column average curve (Figure 8 black) also appears to be slow, excessive, and relatively smooth. In the blue band where there is a problem, the column average curve (blue) of the original image has abnormal changes in the center field of view and the edge field of view, and the column average of the edge field of view is obviously low. After applying the improved histogram matching method, the column mean curve of the blue band is significantly corrected and appears its proportional relationship with the panchromatic band. The corrected images are shown in Figure 9. By comparing with the uncorrected images, the average value of the multi-spectral band in edge FOV column is effectively corrected, which leads to significant improvement in the RGB color composite image. The improved RGB image eliminates the unbalances at the edge FOV, enhances the image radiation accuracy, and provides the true color composite image with higher color contrast. Figure 10 shows the comparisons of the original and corrected BNU-1 images. It indicates that the uncorrected BNU-1 images have better visual performances than the original images.

Figure 8. Comparisons of DN values before and after matching histogram of the CMOS1 and CMOS2 images in band B1. The red box highlights the DN values from the center columns of CMOS1 and CMOS2 images. The original images are the same as Figure 3. The black curve represents the panchromatic band. The blue and cyan curves represent the B1 band before and after applying the matching histogram method, respectively.
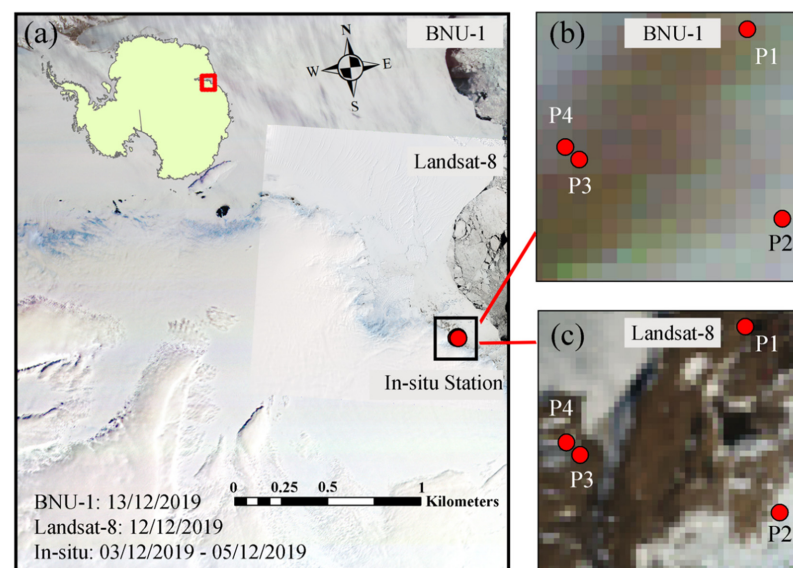

Figure 9. Two true color composite scenes with orbit number 200214500 acquired on 8 October 2019. (**a**,**b**) represent the corrected CMOS1 image and CMOS2 image, respectively.

Uncorrected

Corrected

Figure 10. Comparisons of the original and corrected BNU-1 images. The images shown in (**a**,**d**) are acquired on 6 June 2020 (orbit number: 200020455). The images shown in (**b**,**e**) are acquired on 5 July 2020 (orbit number: 200021032). The images shown in (**c**,**f**) are acquired on 6 June 2020 (orbit number: 200020458).

3.3. Evaluations of the Corrected BNU-1 Images

The spectral information of several typical ground objects was collected at four ground locations which are near Zhongshan Station, East Antarctica in December 2019 (Figure 11). The land cover information and acquisition time of spectral information are shown in Table 2. A total of 40 spectral signatures from three typical surfaces, including snow, lichen, and rock, were observed. The spectral signatures are compared with the observations of the corrected BNU-1 image. Landsat-8 OLI imagery is also used for ground verification due to it having comparable spectral wavelength range at RGB bands and panchromatic bands as BNU-1 imagery. Two images are used to calculate the corresponding radiance at the ground locations. One is the BNU-1 image acquired on 13 December 2019. The other is the Landsat-8 OLI image acquired on 12 December 2019. Both images are chosen since their acquisition time is the closest to the ground spectrum collection time in the field.

Figure 11. Four ground field locations in East Antarctica. The red box in (a) shows the location of the ground fields in Antarctica. The black box in (**a**) shows the spatial region where the 10,000 random point pairs were generated for further assessment. (**b**,**c**) shows four ground field locations in East Antarctica superimposed on top of true color composite images (**a**) Landsat-8 OLI acquired on 12 December 2019 and (**b**) the corrected BNU-1 acquired on 13 December 2019.

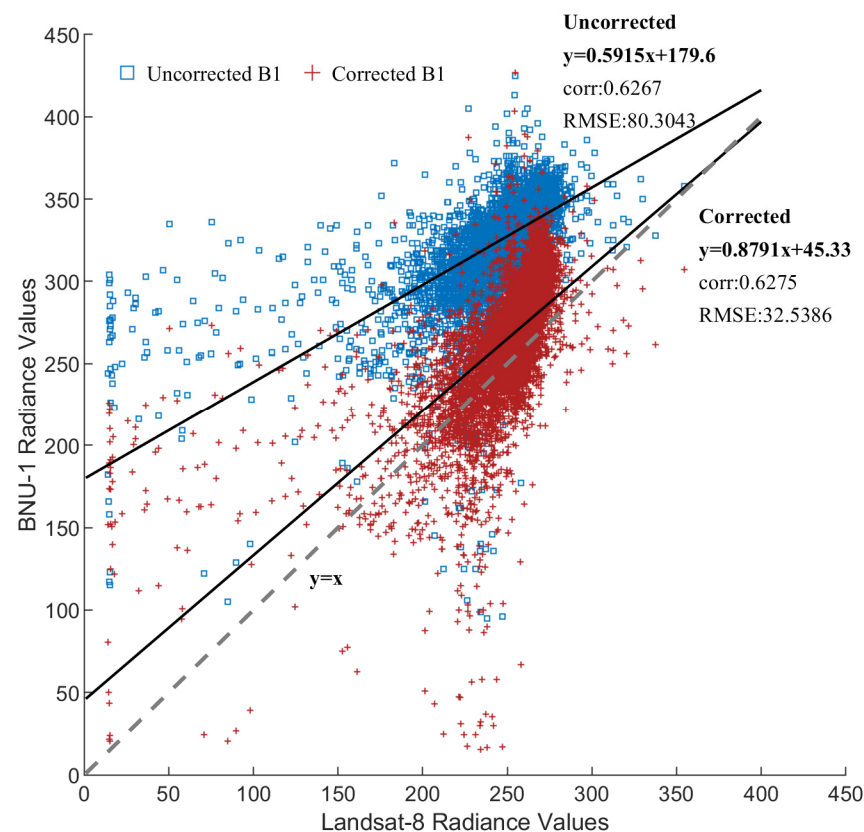**Table 2.** The information of four ground locations near Zhongshan Station, East Antarctica.

Stn NO.	Acquisition Time	Land Cover	The Amount for Data
P1	3 December 2019	Rock	12 spectral signatures
P2	5 December 2019	Snow	10 spectral signatures
P3	9 December 2019	Rock	10 spectral signatures
P4	9 December 2019	Lichen	8 spectral signatures

The evaluations of spectral radiance from original, corrected BNU-1 image and Landsat8 OLI image by using ground observations are shown in Table 3. Compared to the uncorrected images, the spectral radiances of the corrected images remain unchanged in the panchromatic band. The spectral radiances of green (B2) and red (B3) bands are slightly increased, with a general increase of 1–20 $W/m^2/\mu m/sr$. The most significant increase is detected in the blue (B1) band, with an increase of 20–70 $W/m^2/\mu m/sr$. The radiances are most increased on high-reflectance surfaces, such as ice, while they increase less on surfaces with low reflectance, such as rock and lichen. In comparison with the Landsat8 OLI image of the same band, the uncorrected BNU-1 image had slightly higher spectral radiances of low-reflectance surfaces in the green and red bands, such as rocks and lichens, while the radiance in the blue band is much lower than the OLI image. This result indicates that the spectral radiances of uncorrected BNU-1 image have a significant deviation in the blue band. After correction, the radiances of the corrected BNU-1 image in the blue band are consistent with the red and green bands, both being higher than the OLI image. On high-reflectance snow surfaces, the radiances of the uncorrected image in the blue, red, and green bands are significantly lower than the OLI image, while the radiances of the corrected BNU-1 image are close to the OLI image. All the above results indicate that the corrected BNU-1 image has better consistency with the OLI image than the uncorrected one. Compared with the ground radiance measurements, the radiances of corrected BNU-1 image are consistent across all bands with OLI and closely matched with the ground observations on the high-reflectance snow surface. On the low-reflectance surfaces, the corrected BNU-1 image and OLI image are both significantly higher than ground measurements. The underestimation of radiances in the BNU-1 and OLI images may be due to the difference in spatial scale between satellite remote sensing images and ground observations. Due to the uniform characteristic in the snow surface, the scale effect is not significant on the surface with high reflectance. Therefore, the underestimations of radiances of the BUN-1 and OLI images are not detected.

Table 3. Evaluations of spectral radiance from original, corrected BNU-1 image and Landsat8 OLI image by using ground observations. (Unit: $W/m^2/\mu m/sr$).

Stn NO.	Band	Original	Corrected	Landsat	Ground
P1	P	145.36	145.36	111.88	78.38
	Blue	136.89	177.16	116.89	51.18
	Green	155.07	169.57	114.11	75.99
	Red	134.49	148.17	113.32	81
P2	P	230.82	230.82	229.69	233.63
	Blue	241.23	313.07	313.46	288.15
	Green	229.06	236.46	253.85	246.95
	Red	176.39	198.56	209.92	200.21
P3	P	123.03	123.03	85.07	65.04
	Blue	110.80	134.69	119.98	48.35
	Green	103.72	106.95	98.81	66.31
	Red	98.22	96.55	88.73	64.44
P4	P	135.31	135.31	100.86	23.19
	Blue	116.66	144.39	126.34	10.86
	Green	115.75	121.55	114.66	21.17
	Red	105.51	106.61	98.98	25.7

Figure 12 shows the comparisons of radiances from the original, corrected BNU-1 image and the Landsat8 image. The BNU-1 and Landsat8 images were acquired in 12–13 December 2019, in East Antarctica. Figure 11 shows the BNU-1 and Landsat8 images. The blue scatters and line represent the linear relationship between the radiance of the original BNU-1 image and the radiance of the Landsat8 image, while the red scatters and line represent the linear relationship between the radiance of the corrected BNU-1 image and the radiance of the Landsat 8 image. As shown in Figure 12, the red scatters distribute closer to 1:1 line than blue scatters, which indicates that the radiances from the corrected BNU-1 image have small errors than the radiances from the uncorrected image. The RMSE decreases from 80.30 to 32.54 W/m^2/μm/sr. All these results indicate that the radiances from the corrected BUN-1 image is closer to the radiances from the Landsat 8 image than the original BNU-1 image.

Figure 12. Comparisons of radiances from the original, the corrected BNU-1 image and the Landsat8 image. The bule scatters show the relationship between the radiances from the uncorrected BNU-1 image and the Landsat8 image. The red scatters show the relationship between the radiances from the corrected BNU-1 image and the Landsat8 image.

4. Discussion

Rapid and variable cloud cover is one of the major challenges faced by applications of optical remote sensing technology. Establishing a microsatellite constellation to implement a space observation capability with high-frequency and high-resolution observation is a worldwide trend for the future satellite technology. The Planet Company operates a satellite constellation of over 200 active satellites, providing daily global observations with a spatial resolution of 3–5 m every day. The BNU-1 satellite is a type of microsatellite satellite designed by China for polar observation. It achieves the observation capability covering polar areas within 5 days and a resolution of 80 m. Limited by the carrying capacity of the BNU-1 satellite platform, there are still some deficiencies of BNU-1 images, such as the poor control of the satellite attitude resulting in the errors of its geolocation accuracy [10]. The issue of radiometric calibration of satellite sensors also often appears in microsatellite

satellites [17]. Absolute and relative radiometric calibration techniques are widely used in the radiometric calibration of satellite sensors [18].

This study evaluated the radiometric accuracy of the BUN-1 level-0 product. The results showed that systematic biases were detected at the edges of the blue band images obtained by the CMOS1 and CMOS2 sensors of BNU-1, resulting in a noticeable yellow color difference in the BNU-1 true color images. This study developed a relative sensor normalization method, using the panchromatic band radiometric data as references, to correct the radiometric bias in the blue band. The results of the study indicate that the relative sensor normalization method proposed in this study can improve the radiometric accuracy of the BUN-1 level-0 product. The yellow color difference appeared in the uncorrected BNU-1 true color image has been corrected. The corrected true color images have excellent visual performances. The radiances of snow surfaces also have good consistency with ground observations and Landsat-8 images in the red, green, and blue bands. The method proposed in this study corrects the systematic bias of the blue band using only the radiometric characteristics of the panchromatic band, which is simple and easy to be applied for other satellites. Moreover, the radiometric cross-calibration method is a type of widely used radiometric correction method by using images from another satellite to improve the radiometric errors of the target satellite. However, due to different satellite overpass times, the radiometric differences usually existed in the two satellite images from different satellites. Since the BNU-1 images of the panchromatic band and the bule band are observed simultaneously, the proposed method can avoid the radiometric differences caused by different satellite overpass times.

While the relative sensor normalization method we proposed can effectively correct the radiometric bias in the BNU-1 blue band images, it still has some shortcomings. Firstly, for the low-reflectance surfaces, such as rocks and lichens, there are still gaps of radiances between the corrected BNU-1 images and the ground measurements. As shown in Table 3, the radiances of BNU-1 and Landsat 8 images for the low-reflectance surfaces are relatively close and are both higher than ground observations. This may be due to the scale effects of the BNU-1 and Landsat 8 images. The spatial resolutions of BNU-1 and Landsat 8 images are 80 m and 30 m, respectively. It is difficult for a single pixel in the BNU-1 and Landsat 8 images to be composed entirely of low-reflectance surfaces. A pixel may be composed of both low- and high-reflectance surfaces, leading to the higher radiances of BNU-1 and Landsat 8 images over low-reflectance surfaces compared to ground observations. Secondly, although the BNU-1 image corrected by the relative sensor normalization method has significantly improved in visual performances, and the radiances are consistent with the Landsat8 images, the corrected BNU-1 images may still have randoms errors. These errors should be corrected using on-orbit absolute radiometric calibration. In addition, the BNU-1 images corrected by the relative sensor normalization still have some strip noises, which is mainly caused by sensor random errors. Removing the strip noises of the BNU-1 images is another challenge we will face in the future. Currently, deep learning methods are being widely used for image denoising; this may be a new direction for future research.

5. Conclusions

This study developed an on-orbit relative sensor normalization method for satellites and applied this method to the radiometric correction of the BNU-1 satellite. This method uses the radiometric probability density distribution of the BNU-1 panchromatic band as a reference, first correcting the probability density distribution of the blue band radiance. Then, the mean adjustment is used to correct the mean of the blue band radiance after PDF correction, obtaining the corrected radiance in the blue band. This method is applied to correct the BNU-1 images. After correction, the corrected BNU-1 images have better visual effects. The color misrepresentations in the uncorrected BNU-1 images are corrected. Comparisons with ground measured data and Landsat8 image data revealed the following: (1) The radiances of snow surfaces also have good consistency with ground observations and Landsat-8 images in the red, green, and blue bands. (2) The radiance errors of the uncor-

rected BNU-1 images are reduced. The RMSE decreases from 80.30 to 32.54 W/m^2/μm/sr. All these results indicate that the on-orbit relative sensor normalization method proposed in this study can effectively reduce the radiance errors of the BNU-1 images.

References

1. The IMBIE Team. Mass balance of the Greenland Ice Sheet from 1992 to 2018. *Nature* **2020**, *579*, 233–239. [CrossRef]
2. Rignot, E.; Mouginot, J.; Scheuchl, B.; Van Den Broeke, M.; Van Wessem, M.J.; Morlighem, M. Four decades of Antarctic Ice Sheet mass balance from 1979–2017. *Proc. Natl. Acad. Sci. USA* **2019**, *116*, 1095–1103. [CrossRef]
3. Massonnet, F.; Vancoppenolle, M.; Goosse, H.; Docquier, D.; Fichefet, T.; Blanchard-Wrigglesworth, E. Arctic sea-ice change tied to its mean state through thermodynamic processes. *Nat. Clim. Chang.* **2018**, *8*, 599–603. [CrossRef]
4. Spreen, G.; Kaleschke, L.; Heygster, G. Sea ice remote sensing using AMSR-E 89-GHz channels. *J. Geophys. Res. Ocean.* **2008**, *113*, C02S03. [CrossRef]
5. Khan, S.A.; Aschwanden, A.; Bjørk, A.A.; Wahr, J.; Kjeldsen, K.K.; Kjaer, K.H. Greenland ice sheet mass balance: A review. *Rep. Prog. Phys.* **2015**, *78*, 046801. [CrossRef]
6. Friedl, P.; Weiser, F.; Fluhrer, A.; Braun, M.H. Remote sensing of glacier and ice sheet grounding lines: A review. *Earth-Sci. Rev.* **2020**, *201*, 102948. [CrossRef]
7. Beamish, A.; Raynolds, M.K.; Epstein, H.; Frost, G.V.; Macander, M.J.; Bergstedt, H.; Bartsch, A.; Kruse, S.; Miles, V.; Tanis, C.M. Recent trends and remaining challenges for optical remote sensing of Arctic tundra vegetation: A review and outlook. *Remote Sens. Environ.* **2020**, *246*, 111872. [CrossRef]
8. Chen, Z.; Chi, Z.; Zinglersen, K.B.; Tian, Y.; Wang, K.; Hui, F.; Cheng, X. A new image mosaic of Greenland using Landsat-8 OLI images. *Sci. Bull* **2020**, *65*, 522–524. [CrossRef]
9. Dirscherl, M.; Dietz, A.J.; Dech, S.; Kuenzer, C. Remote sensing of ice motion in Antarctica—A review. *Remote Sens. Environ.* **2020**, *237*, 111595. [CrossRef]
10. Zhang, Y.; Chi, Z.; Hui, F.; Li, T.; Liu, X.; Zhang, B.; Cheng, X.; Chen, Z. Accuracy evaluation on geolocation of the Chinese first polar microsatellite (ice pathfinder) imagery. *Remote Sens.* **2021**, *13*, 4278. [CrossRef]
11. Fang, Y.; Wang, X.; Li, G.; Chen, Z.; Hui, F.; Cheng, X. Arctic sea ice drift fields extraction based on feature tracking to MODIS imagery. *Int. J. Appl. Earth Obs. Geoinf.* **2023**, *120*, 103353. [CrossRef]
12. Hui, F.; Kang, J.; Liu, Y.; Cheng, X.; Gong, P.; Wang, F.; Li, Z.; Ye, Y.; Guo, Z. AntarcticaLC2000: The new Antarctic land cover database for the year 2000. *Sci. China Earth Sci.* **2017**, *60*, 686–696. [CrossRef]
13. Itten, K.I.; Meyer, P. Geometric and radiometric correction of TM data of mountainous forested areas. *IEEE Trans. Geosci. Remote Sens.* **1993**, *31*, 764–770. [CrossRef]
14. Thorne, K.; Markharn, B.; Barker, P.S.; Biggar, S. Radiometric calibration of Landsat. *Photogramm. Eng. Remote Sens.* **1997**, *63*, 853–858.
15. Guo, J.; Yu, J.; Zeng, Y.; Xu, J.; Pan, Z.; Hou, M. Study on the relative radiometric correction of CBERS satellite CCD image. *Sci. China Ser. E Eng. Mater. Sci.* **2005**, *48*, 12–28. [CrossRef]
16. Duan, Y.; Chen, W.; Wang, M.; Yan, L. A relative radiometric correction method for airborne image using outdoor calibration and image statistics. *IEEE Trans. Geosci. Remote Sens.* **2013**, *52*, 5164–5174. [CrossRef]

17. Imai, M.; Kurihara, J.; Kouyama, T.; Kuwahara, T.; Fujita, S.; Sakamoto, Y.; Sato, Y.; Saitoh, S.-I.; Hirata, T.; Yamamoto, H. Radiometric calibration for a multispectral sensor onboard RISESAT microsatellite based on lunar observations. *Sensors* **2021**, *21*, 2429. [CrossRef]
18. Kumawat, N.; Babu, K.; Pandya, M.R. On-Orbit Absolute Radiometric Calibration and Uncertainty Analysis of OCM2 Sensor onboard Oceansat-2 Satellite. *Int. J. Remote Sens.* **2023**, *44*, 1254–1279. [CrossRef]